

TAC+: Drastically Optimizing Error-Bounded Lossy Compression for 3D AMR Simulations

Daoce Wang, Jesus Pulido, Pascal Grosset, Sian Jin, Jiannan Tian,
Kai Zhao, James Arhens, and Dingwen Tao

Abstract—Today’s scientific simulations require a significant reduction of data volume because of extremely large amounts of data they produce and the limited I/O bandwidth and storage space. Error-bounded lossy compression has been considered one of the most effective solutions to the above problem. However, little work has been done to improve error-bounded lossy compression for Adaptive Mesh Refinement (AMR) simulation data. Unlike the previous work that only leverages 1D compression, in this work, we propose an approach (TAC) to leverage high-dimensional SZ compression for each refinement level of AMR data. To remove the data redundancy across different levels, we propose several pre-process strategies and adaptively use them based on the data characteristics. We further optimize TAC to TAC+ by improving the lossless encoding stage of SZ compression to efficiently handle many small AMR data blocks after the pre-processing. Experiments on 8 AMR datasets from a real-world large-scale AMR simulation demonstrate that TAC+ can improve the compression ratio by up to $4.9\times$ under the same data distortion, compared to the state-of-the-art method. In addition, we leverage the flexibility of our approach to tune the error bound for each level, which achieves much lower data distortion on two application-specific metrics.



1 INTRODUCTION

The increase in supercomputer performance over the past decades has been insufficient to solve many challenging modeling and simulation problems. For example, the complexity of solving evolutionary partial differential equations scales as $\Omega(n^4)$, where n is the number of mesh points per dimension. Thus, the performance improvement of about three orders of magnitudes over the past 30 years has meant just a $5.6\times$ gain in spatio-temporal resolution [1]. To address this issue, many high-performance computing (HPC) simulation packages [2] (such as AMReX [3] and Athena++ [4]) use Adaptive Mesh Refinement (AMR)—which applies computation to selective regions of most interest—to increase resolution. Compared to the method where a high resolution is applied everywhere, the AMR method greatly reduces the computational complexity and storage overhead; thus, it is one of the most widely used frameworks for many HPC applications [5], [6], [7], [8].

Although AMR can save storage space to some extent, AMR applications running on supercomputers still generate large amounts of data, bringing challenges to data transmission and storage. For example, one Nyx simulation [9] with a resolution of 4096^3 (i.e., 0.5×2048^3 mesh points in the coarse level and 0.5×4096^3 in the fine level) can generate up to 1.8 TB of data for a single snapshot; a total of 1.8 PB of disk storage is needed assuming running the simulation 5 times with 200 snapshots dumped per simulation. Therefore, reducing data size is necessary to lower the storage overhead and I/O cost and improve the overall application performance for running large-scale AMR simulations on supercomputers.

A straightforward way to address this issue is to use data compression. However, traditional lossless compression techniques such as GZIP [10] and Zstandard [11] can only provide a compression ratio by up to $2\times$ for scientific data [12]. On the other hand, a new generation of lossy compressors that can provide strict error control (called “error-bounded” lossy compression) has been developed, such as SZ [13], [14], [15], ZFP [16], MGARD [17], and TTHRESH [18]. Using those error-bounded lossy compressors, scientists can achieve relatively high compression ratios while minimizing the quality loss of reconstructed data and post-analysis, as demonstrated in [19], [20], [21], [22], [23], [24], [25], [26].

Only a few existing contributions have investigated error-bounded lossy compression for AMR applications and datasets. A common approach is to generate uniform-resolution data by up-sampling the coarse-level data and merging them with the finest-level data and then performing compression on the merged data. However, this approach introduces redundant information to the data, which significantly degrades the compression ratio, especially when the up-sampling rate is high or there are multiple coarse levels to up-sample.

Recently, Luo *et al.* introduced zMesh [27], a technique that groups data points that are mapped to the same or adjacent geometric coordinates such that the dataset is smoother and more compressible. However, since zMesh maps data points from different AMR levels to adjacent geometric coordinates and generates a 1D array, it cannot adopt 3D compression which most HPC simulations use. Moreover, zMesh is designed for patch-based AMR data¹ with redundancy across different AMR levels to improve the compression

- Daoce Wang, Sian Jin, Jiannan Tian, and Dingwen Tao (corresponding author) are with Indiana University, Bloomington, IN 47405, USA.
- Jesus Pulido, Pascal Grosset, and James Arhens are with Los Alamos National Laboratory, Los Alamos, NM 87545, USA.
- Kai Zhao is with University of Alabama at Birmingham, AL 35294, USA.

1. The patch-based AMR data redundantly saves the data block to be refined at the next finer level in the current coarse level (will be introduced in detail in Section 2.3).

ratio. However, these coarser levels of redundant data are often not used for post-analysis or visualization and hence can be directly discarded to improve the compression ratio. For this case, the reorganization approach proposed by zMesh cannot improve the data smoothness appropriately (will be illustrated in Section 4).

To solve these issues, we propose TAC that removes the redundant data in coarser level(s) and employs 3D lossy compression for each level. We note that each level may contain many empty/zero regions, where data points are saved in other levels, which may significantly decrease the data smoothness and hence reduce the compression ratio. To this end, TAC either removes these empty regions using adaptive partition strategy or partially pads them with appropriate values, based on the density of empty regions. TAC also has an optimization to reduce the time complexity of removing empty regions.

Although our partition strategies can remove empty regions, there are still several challenges. Specifically, the partition strategies can generate many (e.g., 3,000+) small data blocks with totally different shapes (e.g., 10 different shapes), whereas the SZ compressor performs poorly on relatively small data sets. This is because the SZ compressor uses thousands of Huffman trees to encode these small blocks separately, leading to a low encoding efficiency. A naive solution to the heavy Huffman encoding cost is to linearize/merge the thousands of small blocks into fewer larger blocks and then pass these larger blocks to SZ. This approach can reduce the overhead of the Huffman trees for encoding and hence increase the amount of data encoded together.

However, TAC still has two limitations: (1) Most of the merged small blocks are not adjacent in the original dataset, leading to rapid changes in the data values at the boundaries of these non-neighboring blocks, which impacts the accuracy of SZ’s predictor negatively. (2) Although we can compress data blocks with the same shape together, the SZ compressor must be called multiple times for each shape, resulting in the inevitable low performance of Huffman encoding. To address these limitations, we further optimize TAC to TAC+ by designing a Shared Huffman Encoding (SHE) approach for the SZ compressor. This approach allows individual predictions for each small block while being encoded using a single shared Huffman tree, which can improve the prediction accuracy and compression ratio accordingly.

The main contributions are summarized as follows.

- We propose to leverage 3D SZ compression to compress each level of an AMR dataset separately. We propose a hybrid compression approach based on the following three pre-process strategies and data characteristics.
- We propose an optimized sparse tensor representation to efficiently partition data and remove empty regions for sparse AMR data.
- We propose an enhanced k -d tree approach to reduce the time overhead of removing empty regions.
- We propose a padding approach to improve the smoothness and compressibility of dense AMR data.
- We employ the SHE approach in the SZ compressor to reduce the high time and storage costs of compressing multiple small blocks after the partition.
- We tune the error bound for each AMR level to further improve the compression quality in terms of two

application-specific post-analysis metrics.

- Experiments show that, compared to the state-of-the-art approach zMesh, our proposed AMR compression can improve the compression ratio by up to $4.9\times$ under the same data distortion on the tested datasets.

We evaluate our proposed compression method on eight datasets from three real-world AMR simulation runs. The AMR simulations are well-known, open-source cosmology simulations—Nyx [9]. We compare our method with four baselines including zMesh using generic metrics such as compression ratio and peak signal-to-noise ratio (PSNR) and application-specific metrics such as power spectrum and halo finder. Our code is available at <https://github.com/FabioGrosso/3dAMRcomp>.

In Section 2, we present background information about error-bounded lossy compression, AMR method, k -d tree, and related work on AMR data compression. In Section 3, we describe our proposed pre-process strategies, SHE approach, and hybrid compression. In Section 4, we show the experimental results on different AMR datasets. In Section 5, we conclude our work and discuss the future work.

2 BACKGROUND AND RELATED WORK

2.1 Lossy Compression for Scientific Data

There are two main categories for data compression: lossless and lossy compression. Compared to lossless compression, lossy compression can offer a much higher compression ratio by trading a little bit of accuracy. There are some well-developed lossy compressors for images and videos such as JPEG [28] and MPEG [29], but they do not have a good performance on the scientific data because they are mainly designed for integers rather than floating points.

In recent years there is a new generation of lossy compressors that are designed for scientific data, such as SZ [13], [14], [15], ZFP [16], MGARD [17], and TTHRESH [18]. These lossy compressors provide parameters that allow users to finely control the information loss introduced by lossy compression. Unlike traditional lossy compressors such as JPEG [28] for images (in integers), SZ, ZFP, MGARD, and TTHRESH are designed to compress floating-point data and can provide a strict error-controlling scheme based on the user’s requirements. Generally, lossy compressors provide multiple compression modes, such as error-bounding mode and fixed-rate mode. Error-bounding mode requires users to set an error type, such as the point-wise absolute error bound and point-wise relative error bound, and an error bound level (e.g., 10^{-3}). The compressor ensures that the differences between the original data and the reconstructed data do not exceed the user-set error bound level.

In this work, we focus on the SZ lossy compression (2021 R&D 100 Award Winner [30]) because SZ typically provides a higher compression ratio than ZFP [22], [31] and higher (de)compression speeds than MGARD [31], [32] and TTHRESH [18]. SZ is a prediction-based error-bounded lossy compressor for scientific data. It has three main steps: (1) predict each data point’s value based on its neighboring points by using an adaptive, best-fit prediction method; (2) quantize the difference between the real value and predicted value based on the user-set error bound; and (3) apply a customized Huffman coding and lossless compression.

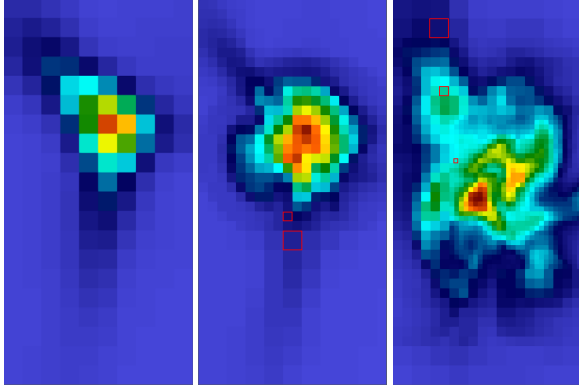


Fig. 1: Visualization (one zoom-in 2D slice) of three key timesteps generated from an AMR-based cosmology simulation. The grid structure changes with the universe’s evolution. The red boxes indicate different resolutions within one AMR level.

2.2 AMR Method and AMR data

AMR is a method of adapting the accuracy of a solution by using a non-uniform grid to increase computational and storage savings while still achieving the desired accuracy. AMR applications change the mesh or spatial resolution based on the level of refinement needed by the simulation and use *finer mesh in the regions with more importance/interest and coarser mesh in the regions with less importance/interest*. Figure 1 shows that during an AMR run, the mesh will be refined when the value meets the refinement criteria, e.g., refining a block when its norm of the gradients or maximum value is larger than a threshold.

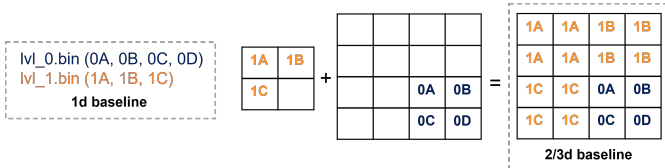


Fig. 2: A typical example of AMR data storage and usage.

Clearly, the data generated by an AMR application are hierarchical data with different resolutions. The data of each AMR level are usually stored separately (e.g., in a 1D array). For example, Figure 2 (left) shows a simple example of two-level AMR data; “0” means high resolution (the fine level) and “1” for low resolution (the coarse level). When the AMR data are needed for post analysis or visualization, users will typically convert the data from different levels to a uniform resolution. In the previous example, we will up-sample the data in the coarse level and combine it with the data in the fine level, as shown in Figure 2 (right).

2.3 Tree-based and Patch-based AMR Data

There are two types of techniques to represent AMR data: patch-based AMR and tree-based AMR [33]. The main difference between them is that the patch-based AMR technique generates AMR data with redundancy across different levels. In other words, the patch-based AMR data structure redundantly saves data blocks to be refined at the next level in the current level, simplifying the computation in the refinement process. By comparison, the tree-based AMR technique organizes the grids on the tree leaves, so there is no redundant data across different levels. But tree-based AMR

data is more complex for post analysis and visualization compared to patch-based AMR data [34].

In this work, we focus on a state-of-the-art patch-based AMR framework AMReX. Note that since the redundant coarser-level data in the patch-based AMR will not often be used in post-analysis, we discard them during compression to improve the compression ratio.

2.4 Existing AMR Data Compression

1D AMR Compression: The main challenge for AMR data compression is that the AMR data is comprehensive and hierarchical with different resolutions. A naive approach is to compress the 1D data of each AMR level separately. However, this approach loses most of the topological/spatial information, which is critical for data compression. zMesh [27] is a state-of-the-art AMR data compression based on the 1D approach. Different from the naive 1D approach, zMesh reorganizes the 1D data based on each point’s coordinate in the 2D layout; in other words, zMesh puts the points neighbored in the 2D layout closer in the 1D array. It can increase the data smoothness/compressibility to benefit the following 1D compression such as SZ on patch-based AMR data with redundancy across different AMR levels. However, zMesh does not leverage high-dimensional compression, while many previous studies [14], [35] proved that leveraging more dimensional information (e.g., spatial/temporal information) can significantly improve the compression performance. Moreover, it only focuses on 2D AMR data. Our work aims to leverage high-dimensional data compression and supports 3D AMR data.

High-dimensional AMR Compression: Similar to the idea described in Section 2.2, a straightforward way to leverage 3D compression on 3D AMR data is to compress different levels together by up-sampling coarse levels. However, this approach must handle extra redundant data generated by the up-sampling process. As shown in Figure 2, 1A, 1B, and 1C are redundant points in the compression. Note that the storage overhead of these redundant points will be higher when more data are in the coarse levels or the up-sampling rate is higher, especially for 3D AMR data. This is because we only need to duplicate one point from the coarse level 4 times for 2D AMR data but 8 times for 3D AMR data, with an up-sampling rate of 2. Another limitation of this approach is that it cannot apply different compression configurations (e.g., error bound) to different AMR levels. This is because after up-sampling all data points will have the same importance. However, the purpose of using the AMR method is to set different interests to different AMR levels, so the error bound for each AMR level can be chosen adaptively.

2.5 k -D Tree for Particle Data Compression

k -d tree [36] is a binary tree in which every node represents a certain space. Without loss of generality, for the 3D case, every non-leaf node in a k -d tree splits the space into two parts by a 2D plane associated with one of the three dimensions. The left subspace is associated with the left child of the node, while the right subspace is associated with the right child. k -d tree is commonly used in particle data compression [37], [38], [39] to locate each particle and remove empty regions. Specifically, a k -d tree keeps dividing the space in between

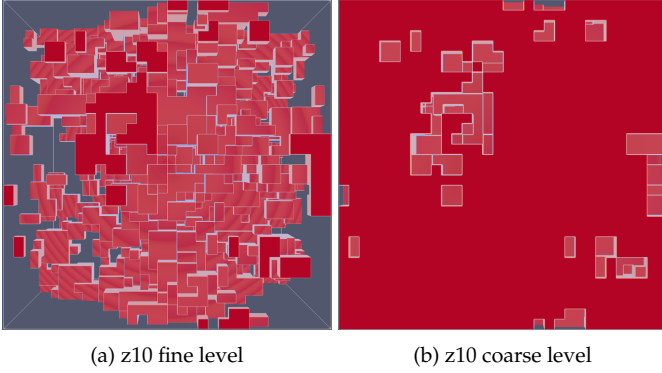


Fig. 3: Visualization of data distributions of an example AMR data “z10”, where z = redshift. Non-empty regions are shown in red.

along one dimension until the space is empty or contains only one particle. We will optimize the classic k -d tree and use it to remove empty regions and increase the compressibility for each AMR level (to be detailed in Section 3.3).

3 OUR PROPOSED DESIGN

In this section, we propose a pre-processing approach for AMR data to leverage high-dimensional SZ lossy compression at each AMR level. Specifically, we propose three pre-process strategies to mitigate the issue of irregular data distribution. We further propose Shared Huffman Encoding (SHE) and integrate it into the SZ compressor to further improve the compression performance for AMR data. We also propose an adaptive approach to select the best-fit pre-processing strategy based on the data density of each level.

3.1 Ghost-Shell Padding for High-density Data

To compress the AMR data in 3D, besides the aforementioned 3D baseline, we can also compress each level separately in 3D. In that way, however, the data will be split into multiple levels, and each level will have many empty regions and an irregular data distribution, as shown in Figure 3. A naive solution to handle the irregular 3D data is to fill the empty regions with zeros and pass a large 3D block to the compressor. Although the padded zeros will increase the size of data for compression, for high-density data such as z10’s coarse level shown in Figure 3b (i.e., about 77% density), the size overhead will be small.

However, these padded zeros can also greatly reduce the performance of compression, especially for prediction-based lossy compression such as SZ, because these zeros can significantly affect the prediction accuracy of SZ, resulting in high compression errors on the boundaries, as shown in Figure 5a. More specifically, as mentioned in Section 3.2, SZ uses each point’s neighboring points’ values to predict its value. Thus, for those boundary points which are adjacent to padded zeros, SZ will involve zero(s) in the prediction, while the actual values of these empty regions are typically non-zeros (saved in other AMR levels), which will seriously mislead the prediction.

To eliminate the above issue of padding zeroes, we propose to use a ghost-shell padding strategy (GSP) to diffuse neighboring values to a padding layer. Figure 4 illustrates the high-level idea, and the detailed algorithm is described in Algorithm 1. Specifically, we first partition the data into

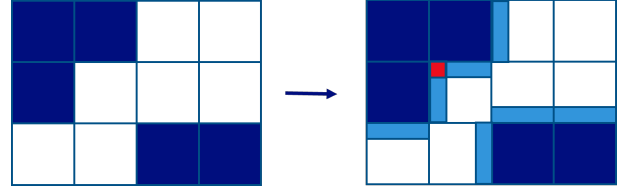


Fig. 4: A 2D example of GSP approach. Non-empty blocks are in navy blue; padded blocks are in light blue/red; padded blocks based on more than one non-empty neighbor are in red.

Algorithm 1: Proposed Ghost Shell Padding Method

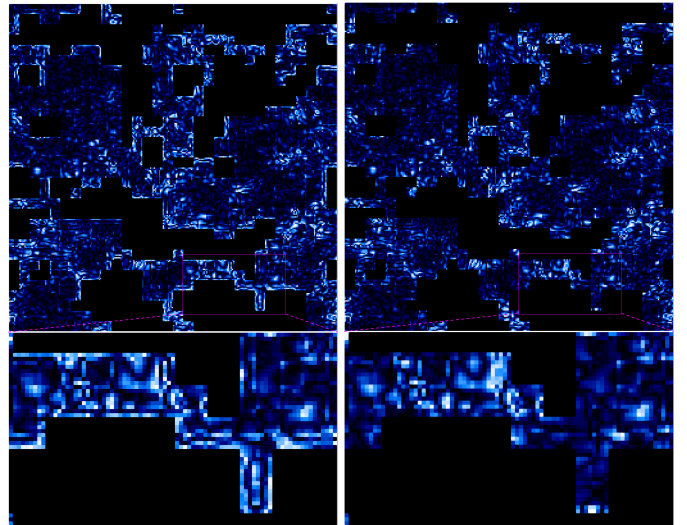
```

Input: Data,  $x$ ,  $y$ 
Output: Data after padding
1 for each unit block  $b_i$  do
2   if  $b_i$  is empty and  $b_i$  has non-empty neighbor then
3     for each non-empty neighbor  $n_j$  do
4       pad slice = avg (first  $y$  slices of  $n_j$  next
5         to  $b_i$ );
6       if overlap edge then
7         | pad = pad/2;
8       else if overlap corner then
9         | pad = pad/3;
10      else
11        | continue;
12      end
13      add an  $x$ -layers pad slice to  $b_i$  next to
14         $n_j$ ;
15    end
16  end
17 return padded Data

```

unit blocks and then pad each empty unit block by using the average of its non-empty neighbors’ boundary data values.

Note that some empty unit blocks have more than one non-empty neighbor such as the red box shown in Figure 4. For these blocks, we will use the average value of all its neighbors for padding. Correspondingly, we will remove these padded values in the decompression based on the saved padding information. Note that since the padding process is only for non-empty blocks, this metadata overhead is almost negligible for high-density data (e.g., 0.1%).



(a) ZF (CR=156.7, PSNR=32.8dB) (b) GSP (CR=161.3, PSNR=33.5dB)
 Fig. 5: Visual comparison (one slice) of compression errors of two approaches using SZ based on Nyx’s “baryon density” field (i.e., z10’s coarse level, 77% density). Brighter means higher compression error. The error bound is the relative error bound of 6.7×10^{-3} .

After padding, each boundary point will be predicted using the average of all the boundary data in the unit block(s) to which it belongs or is neighbored. As shown in Figure 5, compared to the zero-filling (ZF) approach, GSP can significantly reduce the overall compression error, especially for the boundary data. Moreover, the GSP approach can provide a similar compression ratio to the ZF approach on this high-density data and hence a better rate-distortion. A detailed evaluation will be presented in Section 4.

3.2 Optimized Sparse Tensor Representation for Low-density Data

When most of the regions in the data are empty (e.g., about 77% of the data is empty in Figure 3a), the large amount of padded data would greatly increase the size of data for compression, resulting in a low compression ratio.

To solve this issue, we propose to use a naive sparse-tensor-based approach (called **NaST**) to remove the empty regions, as shown in Figure 6. NaST includes four main steps in the compression process: (1) partition the 3D data into multiple unit blocks, (2) remove the empty blocks, (3) linearize the remaining 3D blocks into a 4D array, and (4) pass the 4D array to the compressor. Note that in the decompression process, we will put the unit blocks from the decompressed 4D array back into the original data.

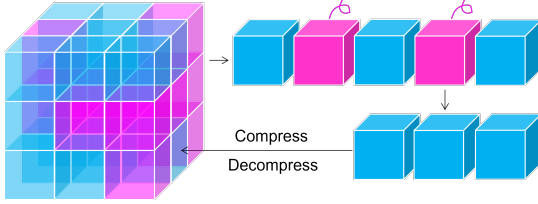


Fig. 6: Workflow of the naive sparse tensor (NaST) method (empty regions marked in pink and non-empty regions marked in blue).

However, in order to completely remove the empty regions to form a sparse representation, the unit block size needs to be relatively small compared to the input data size (e.g., 16^3 vs. 512^3), resulting in a high proportion of data on the boundary. While the linearized unit blocks are usually not adjacent in the original data, so the boundary data between them are not smooth. Thus, it is harder for prediction-based compressors such as SZ to predict the boundary data values. As a result, the NaST method without optimizing the boundary data would have low compression performance.

To address the above problem, we propose an optimized sparse tensor representation (called **OpST**) to effectively remove the empty regions as well as maintain a relatively large unit block size so as to reduce the portion of boundary data. A detailed description of our algorithm can be found in Algorithm 2. We use a 2D example to demonstrate our approach, as illustrated in Figure 7. Specifically, (1) we partition the data into many small unit blocks. (2) For each unit block, we use the dynamic programming method to initiate an array BS to save the dimension/size of the maximum square whose bottom-right corner is that unit block (line 6, which will be discussed in the next paragraph). (3) We extract the sub-blocks (composed of multiple unit blocks) from the original data according to the sizes saved in BS (lines 13). (4) Since the original data will be changed after the

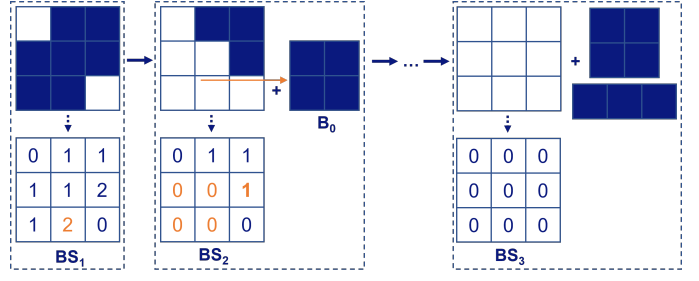


Fig. 7: A 2D example of our proposed OpST approach. The sub-blocks are extracted according to our optimized sizes saved in BS . E.g., a 2-by-2 sub-block B_0 is extracted according to $BS_1[2][1]$.

extraction, we need to partially update BS based on $maxSide$ (lines 14, will be discussed later). We loop (3) and (4) from the bottom-right corner to the top-left corner until the original data is empty. (5) After extracting all the sub-blocks, we put them into multiple 3D arrays (to be compressed) based on their sizes. Note that the sub-blocks with the same size will be merged into the same array for easy compression.

Algorithm 2: Proposed Optimized Sparse Tensor Method

Input: Sparse 3D data S
Output: multiple 4D array D_n

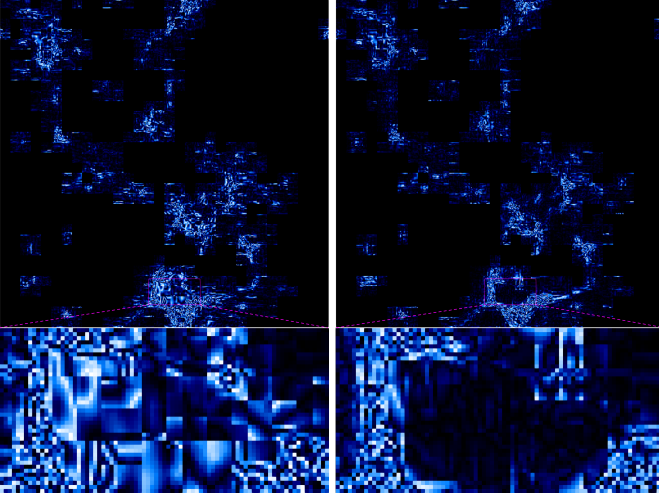
```

1 for each unit block  $b(x, y, z)$  do
2   if  $b(x, y, z)$  is non-empty then
3     if  $x$  is 0 or  $y$  is 0 or  $z$  is 0 then
4        $BS(x, y, z) = 1$ 
5     else
6        $BS(x, y, z) = \min(BS(x-1, y, z), BS(x, y-1, z), BS(x, y, z-1), BS(x-1, y-1, z), BS(x, y-1, z-1), BS(x-1, y, z-1), BS(x-1, y-1, z-1)) + 1$ ;
7       /*  $BS(x, y, z)$  is the dimension size of the maximum cube whose bottom right rear corner is the unit block with index  $(x, y, z)$  in the original data */
8        $maxSide = \max(maxSide, BS(x, y, z))$ 
9   end
10 end
11 for each unit block  $b(x, y, z)$  do
12   if  $BS(x, y, z) \geq 1$  then
13      $size = BS(x, y, z)$ 
14      $D_{size} \leftarrow S((x-size : x) * blkSize, (y-size : y) * blkSize, (z-size : z) * blkSize)$ ; /* put the sub-block to the according to 4D array */
15      $b(x-size : x, y-size : y, z-size : z) \leftarrow empty$ 
16      $BS(x-size : x, y-size : y, z-size : z) = 0$ 
17      $BS = updateBs(BS, x, y, z, maxSide)$ 
18   end
19 end
20 return  $D_n$ 

```

When initializing the BS in step (2), we start with the $b'[i][j]$ with $i = 0$ or $j = 0$ (i.e., on the top-left edge), where $b'[\cdot][\cdot]$ are the unit blocks: if $b'[i][j]$ is empty, we will set $BS[i][j]$ to 0 otherwise 1. For the remaining unit blocks, if it is empty, $BS[i][j]$ will be 0; otherwise, $BS[i][j]$ will be set to 1 plus the minimum value among its three neighboring blocks (i.e., upper block, left block, and upper-left block). In other words, we have $BS[i][j] = 1 + \min(BS[i][j-1], BS[i-1][j], BS[i-1][j-1])$ for the 2D case. For example, $BS_1[2][1]$ is 2 because all its upper-left neighbors are 1 (as shown in Figure 7). However, both $BS_1[1][1]$ and $BS_2[1][2]$ can only reach 1 because one of their neighbors is set to 0, having no chance to form a sub-block with the size of 2.

Moreover, as mentioned in step (3), we need to update



(a) NaST(CR=245, PSNR=77.5dB) (b) OpST(CR=248, PSNR=78.0dB)

Fig. 8: Visual comparison (one slice) of compression errors of two approaches using SZ based on Nyx’s “baryon density” field (i.e., z10’s fine level, 23% density). Brighter means higher compression error. The error bound is the relative error bound of 7.2×10^{-4} .

BS after each extraction. Specifically, for each sub-block we extract, we have to set its corresponding values in BS to zeros. For instance, as shown in Figure 7, after we extract a 2-by-2 sub-block B_0 at $BS_1[2][1]$, we need to set $BS_2[1][0]$, $BS_2[1][1]$, $BS_2[2][0]$, and $BS_2[2][1]$ to zeros. In addition, we also need to recalculate a part of BS (line 17 in Algorithm 2) because the extraction could influence other BS values. For example, we need to recalculate $BS_2[1][2]$ (marked in bold orange) after extracting B_0 . Note that this update is a partial update as the BS values to be updated will be bounded by $maxSide$ which is the dimension size of the largest cube in the dataset (line 7).

Similar to NaST, in decompression, we will put the sub-blocks back to reconstruct the data based on the saved coordinates. Note that after our optimization, each sub-block size will be relatively large (e.g., 96^3 vs the original data size of 512^3), the overhead of saving the coordinates of all the sub-blocks will be negligible (e.g., 0.1%).

Finally, we show a visual comparison of the compression quality between NaST and OpST in Figure 8. Note that both use SZ with the same error bound. Brighter means more errors. We can observe that compared to the NaST method, OpST can significantly reduce the overall compression error, especially for the data points on the boundary. It is worth noting that even with a lower error, our OpST can still provide a higher compression ratio than NaST. This is because our proposed optimization will generate larger sub-blocks, which provide more information for prediction-based lossy compressors such as SZ to achieve better rate-distortion. A detailed evaluation will be shown in Section 4.

3.3 Adaptive k -D Tree for Medium-density Data

The OpST approach proposed for low-density data, however, has a high computation overhead, especially when the data is relatively dense. This is because, on one hand, OpST needs to update BS based on $maxSide$ for each extraction of a sub-block, while the larger the $maxSide$, the more values in BS that need to be updated; on the other hand, $maxSide$ is the dimension size of the largest non-empty cube in the dataset,

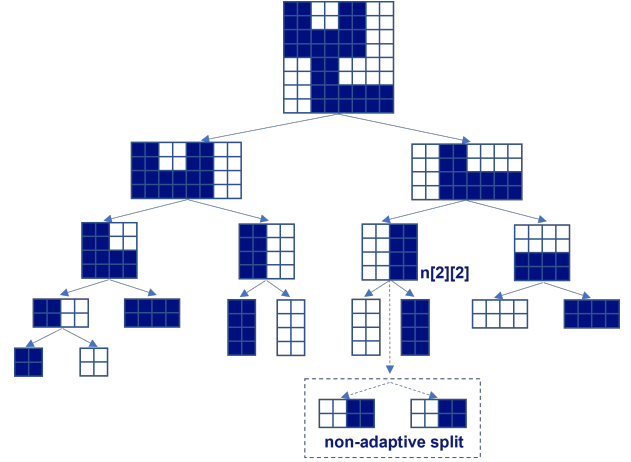


Fig. 9: 2D example of adaptive k -D tree. Sub-block will be adaptively split to effectively remove empty regions and get bigger full sub-blocks, which is highly related to the density of the dataset. Thus, the time complexity of OpST can be expressed as $O(N^2 \cdot d)$, where N is the unit block number and d is the density. Note that here density describes how dense the data is. For example, the density of 77% means that 23% of the data is empty. Clearly, when the density of an AMR level is relatively high, using OpST will be relatively time-consuming.

Algorithm 3: Dynamic k -D Tree

Input: data block d , counts information
Output: k -d tree

```

1 node.count ← counts information;
2 if  $d$  is empty or  $d$  is full then
3   continue ; /* stop splitting */
4 else
5   if  $d$  is a cube then
6     split  $d$  equally into 8 oct-blocks:  $s_1, \dots, s_8$ ;
7     get the counts  $c_1, \dots, c_8$  for  $s_1, \dots, s_8$ ;
8     find the maxDiff partition  $d_1, d_2$ ;
9     node.left = AKDTree( $d_1$ , four  $c_i$  of  $d_1$ );
10    node.right = AKDTree( $d_2$ , four  $c_i$  of  $d_2$ );
11  else if  $d$  is a flat cuboid then
12    get the counts  $c_1, \dots, c_4$  from counts
    information;
13    find the maxDiff partition  $d_1, d_2$ ;
14    node.left = AKDTree( $d_1$ , two  $c_i$  of  $d_1$ );
15    node.right = AKDTree( $d_2$ , two  $c_i$  of  $d_2$ );
16  else if  $d$  is a slim cuboid then
17    get the counts  $c_1, c_2$  from counts information;
18    split  $d$  along the largest dimension to get
     $d_1, d_2$ ;
19    node.left = AKDTree( $d_1, c_1$ );
20    node.right = AKDTree( $d_2, c_2$ );
21  end
22 return node;
```

To address the above high overhead issue of OpST, we propose an adaptive k -d tree, called **AKDTree**, to remove empty regions and extract sub-blocks (containing multiple unit blocks). AKDTree has a lower time complexity of $O(\frac{1}{3}N \cdot \log N)$ (will be discussed later). Figure 9 shows a simple 2D example. Specifically, (1) we partition the data into small unit blocks. (2) We use a tree to hierarchically represent the whole data. Each node in the tree is associated with a sub-block of the data. Moreover, each node stores the number of non-empty unit blocks in the sub-block associated with the node. (3) For each node, we split its associated sub-block from the middle along one dimension to form

two sub-blocks for its two children. Note that we select one dimension which can maximize the difference of the numbers of non-empty unit blocks of the two children (will be discussed in the next two paragraphs). (4) We keep splitting a node until it has no empty unit block or itself is empty. (5) Once finishing the construction of the tree, we collect all the leaf nodes and send them to the compressor. Note that a non-empty leaf node does not have any empty unit block; otherwise, it will keep splitting. Thus, a leaf node must be an empty or full node, as shown in Figure 9. The detailed algorithm is described in Algorithm 3.

As mentioned in step (3), we are distributing the non-empty unit blocks unevenly to two children for each node because we attempt to get as many leaf nodes with large sub-block sizes as possible. If we keep splitting sub-blocks in a fixed way, for instance, first split along the x -axis, second split along the y -axis, third split along the x -axis, fourth split along the y -axis, and so on, we will get a 2-by-2 sub-block for the node $n[2][2]$ as shown in the dashed box, while its largest possible sub-block could be 4 by 2 as shown in Figure 9.

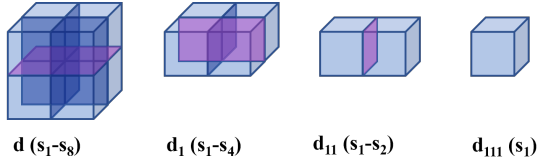


Fig. 10: Example of adaptive splitting, different shapes will have a different number of choices for splitting.

To select one of the dimensions to unevenly distribute its non-empty unit blocks to the two children, we now present our dynamic splitting approach. We categorize nodes into three different types: “cube” nodes, “flat” nodes, and “slim” nodes, whose dimension ratios are 1:1:1, 2:2:1, 2:1:1, respectively. First of all, for the cube node d , we first divide it into eight oct-blocks, i.e., s_1, s_2, \dots, s_8 (as shown in Figure 10), each sized $\frac{n^3}{2}$. Here n is the dimension size of the original data. Then, we can get the counts of non-empty unit blocks of the eight oct-blocks, i.e., c_1, c_2, \dots, c_8 . After that, we will decide along which dimension to split the cube node d based on the counts. Specifically, we can calculate the following three differences:

$$\begin{aligned} \text{diff}_x &= |c_1 + c_3 + c_5 + c_7 - c_2 - c_4 - c_6 - c_8|, \\ \text{diff}_y &= |c_1 + c_2 + c_5 + c_6 - c_3 - c_4 - c_7 - c_8|, \\ \text{diff}_z &= |c_1 + c_2 + c_3 + c_4 - c_5 - c_6 - c_7 - c_8|. \end{aligned}$$

Finally, we compare these three values and choose the dimension with the maximum difference to split. For example, if the maximum difference is diff_z , we will split d along the z -axis (i.e., the pink 2D plane shown in Figure 10) and get two flat nodes d_1 and d_2 . For the flat nodes such as d_1 , we can reuse c_1, \dots, c_4 to decide whether to split d_1 along the x -axis or y -axis by choosing the larger one among the following two differences.

$$\text{diff}_x = |c_1 + c_3 - c_2 - c_4|, \quad \text{diff}_y = |c_1 + c_2 - c_3 - c_4|.$$

For the slim nodes such as d_{11} , we simply split it along the x -axis to get two cube nodes s_1 and s_2 . This process (i.e., cube nodes \rightarrow flat nodes \rightarrow slim nodes) in step (3) will be looped until the node becomes a leaf node (empty or full).

Algorithm 4: SZ compression with SHE

```

Input: multiple data block  $D_{1..n}$ 
Output: compressed data  $S$ 
1 quantCode  $Q$ , regreCoeff  $R$ , compressed data  $S$ ;
2 for each data block  $D_i$  do
3   quantCode block  $q_i$ , regreCoeff block  $r_i$ ;
4    $q_i, r_i = \text{SZ.compress}(D_i)$ ;
5    $Q.append(q_i)$ ;
6    $R.append(r_i)$ ;
7 end
8  $S \leftarrow \text{HuffmanEncode}(Q)$ ;
9  $S \leftarrow \text{HuffmanEncode}(R)$ ;          /* end compression */
10 return  $S$ ;

```

Note that based on the above description, the counting process is required for every three nodes in each three path (i.e., only for the “cube” nodes). Thanks to this dynamic splitting approach, we can lower the time complexity of the AKDTree algorithm to $O(\frac{1}{3} \cdot N \cdot \log N)$, where N is the number of unit blocks while extracting as many relatively large sub-blocks without empty unit block as possible.

In addition, after the dynamic splitting, we will have a series of sub-blocks with the same size but in different directions (e.g., 2:2:1, 2:1:2, 1:2:2). We will align the sub-blocks with the same size based on their splitting dimensions (instead of in-memory transposing them), merge them into an array, and feed multiple merged arrays to the compression.

3.4 Shared Huffman encoding

As mentioned in Section 1, 3.3 and 3.2, the OpST and AKDtree methods collect and linearize the data blocks with the same shape into a 4D array and send it to SZ. However, poor data locality/smoothness between non-neighbored data blocks can negatively impact prediction accuracy, resulting in low data quality. A potential solution could be compressing each data block individually using SZ. However, this approach would result in low Huffman encoding efficiency because the entire dataset would be divided into many small blocks, requiring SZ to build a separate Huffman tree for each of these small blocks. In other words, the original SZ method either requires predicting and encoding small blocks together (by forcing them merged into 4D arrays), leading to low prediction accuracy or predicting and encoding each small block separately, which results in high Huffman encoding overhead. Furthermore, even if the data blocks with the same shape can be compressed together, the data blocks with different shapes still need to be compressed separately, resulting in low Huffman encoding performance and a high time cost of launching SZ multiple times.

To this end, for OpST and AKDtree, we propose a shared Huffman encoding technique to predict data blocks separately while encoding them together using a single shared Huffman tree. The detail is shown in Algorithm 4. Each data block is first predicted and quantized separately. Then, the quantization codes and regression coefficients of each data block are aggregated to build a shared Huffman tree and encoded at one time. This approach improves the prediction performance of SZ without introducing high time overhead to the encoding of SZ. As shown in Figure 3.4, compared to the original AKDtree, AKDtree with SHE can significantly reduce the overall compression error, especially for the data located at the boundary of data blocks, leading to significant

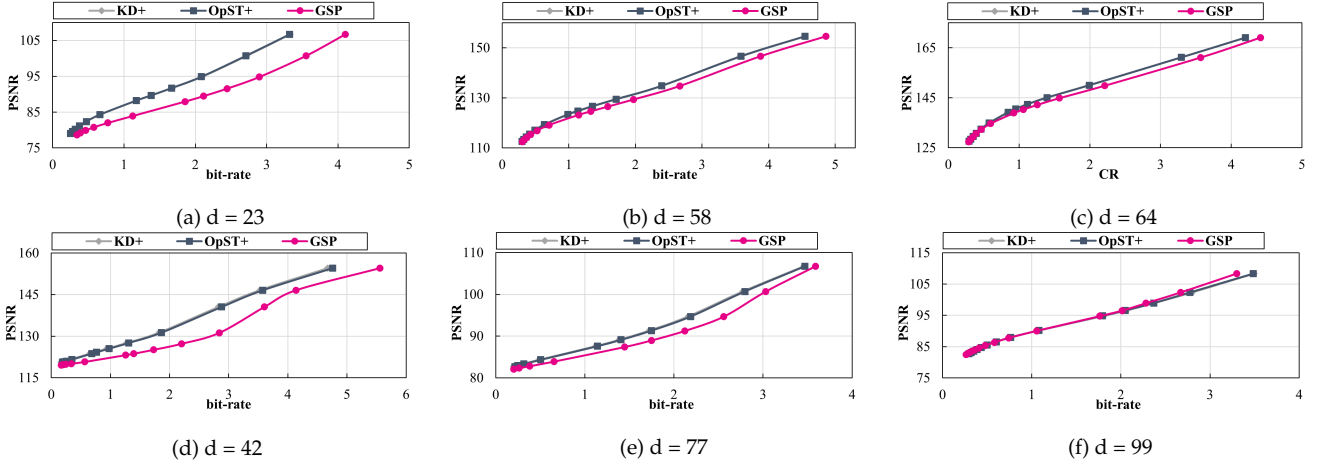
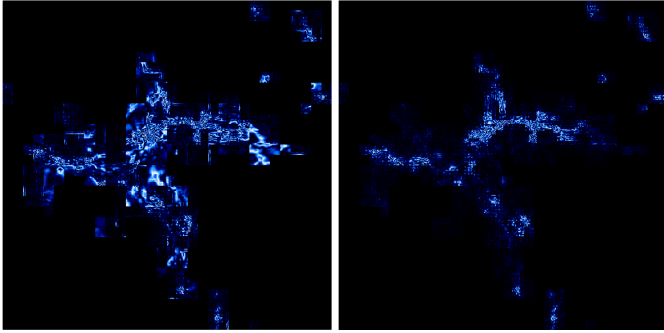


Fig. 11: Compression performance comparison of GSP, OpST, and AKDTree on six datasets with different densities.



(a) AKDtree (CR=222, PSNR=78.5dB) (b) AKDtree + SHE (CR=231, PSNR=79.6dB)

Fig. 12: Visual comparison (one slice) of compression errors of two approaches using SZ based on Nyx’s “baryon density” field (i.e., z10’s fine level, 23% density). Brighter means higher compression error. The error bound is the relative error bound of 4.8×10^{-4} .

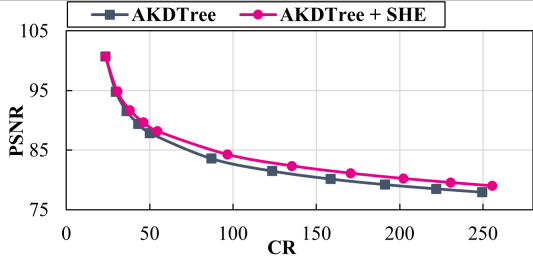


Fig. 13: Comparison of original AKDTree and AKDTree with SHE on Nyx’s “baryon density” field (i.e., z10’s fine level, 23% density).

PSNR improvement, as shown in Figure 13. Furthermore, the use of SHE reduces the number of Huffman trees needed for the data (since we do not need separate Huffman trees for different block shapes), thereby improving encoding efficiency and compression ratio.

3.5 Hybrid Compression Strategy

In this section, we propose a solution to adaptively choose a best-fit compression strategy from our proposed *OpST with SHE* (*OpST+*), *AKDTree with SHE* (*AKDTree+*), and GSP based on the data characteristics (i.e., data density). According to Section 3.2 and 3.3, *OpST+* is more suitable for sparse (i.e., low-density) data, while *AKDTree+* is designed to address the high time overhead of *OpST+* when the density of data increases. Thus, there should be a data-density threshold to determine when to use *OpST+* or *AKDTree+*.

To decide the threshold T for switching between *OpST+* and *AKDTree+*, we perform a series of experiments, as shown in Figure 11. The figure shows that *OpST+* and *AKDTree+* have almost identical compression performance in terms of bit-rate and PSNR on all six datasets/levels (from different timesteps) with different densities. Moreover, Figure 14 shows the time costs of *OpST+* and *AKDTree+* (excluding compression). The figure demonstrates that the time of *AKDTree+* is relatively stable, while the time of *OpST+* increases linearly with the increase of data density. Overall, the only criterion for selecting *OpST+* or *AKDTree+* is the time cost rather than the compression performance. This is consistent with our previous design aim, that is, *AKDTree* is mainly designed to address the high time overhead issue of *OpST+*. Since *OpST+* and *AKDTree+* have a similar speed when the density is around 50%, we propose to choose $T = 50$ for choosing *OpST+* or *AKDTree+*.

According to Section 3.1, GSP is designed to effectively handle the AMR level with high data density to prevent the negative impact of data partitioning without the use of SHE. In contrast, the data partition methods such as *AKDTree* require small blocks to be compressed together without SHE, which can significantly decrease prediction accuracy, as shown in Section 3.4. However, the negative impact on prediction accuracy caused by the partition can be eliminated by using SHE to compress each small block produced by the partition, which incurs little overhead, while GSP introduces significant overhead to the data size. As shown in Figure 11, *OpST+* and *AKDTree+* outperform GSP across all the densities. As a result, the improved partition strategies using SHE can be a viable alternative to GSP for all levels.

In summary, our proposed hybrid compression approach

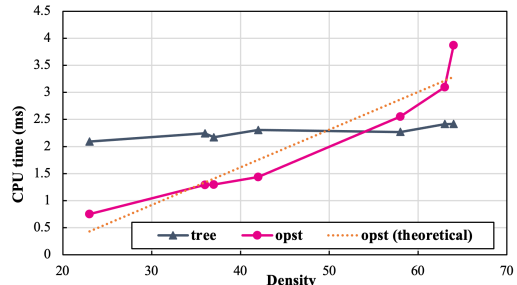


Fig. 14: Time overhead comparison of *OpST* and *AKDTree* on different datasets with different densities.

is described as follows.

- 1) When the density is smaller than $T = 50\%$, we use OpST+ to remove empty regions and then compress;
- 2) When the density is larger than $T = 50\%$, we use AKDTree+ to remove empty regions and then compress.

4 EXPERIMENTAL EVALUATION

4.1 Experimental Setup

Test data. Our evaluation mainly focuses on the AMReX framework [3], particularly the Nyx cosmology simulation [9]. Nyx is a state-of-the-art extreme-scale cosmology code using AMReX, which generates six fields including baryon density, dark matter density, temperature, and velocities (x , y , and z). We use nine datasets generated by three real-world simulation runs with different numbers of AMR levels, simulating a region of 64 megaparsecs (Mpc). For this data, Z is equal to the redshift, i.e. the displacement distant galaxies and celestial objects, as seen in Tab 1.

Specifically, the first run has two levels of refinement, with the coarse level of 256^3 grids and the fine level of 512^3 grids. We’ve collected four timesteps with the finest level density from 23% to 64%. The second run has a maximum of four levels of refinement. It was initially configured at the resolution of 128^3 and gradually refined to 1024^3 . This run collected three timesteps with the finest-level resolution of 256^3 (two levels), 512^3 (three levels), and 1024^3 (four levels), respectively. The density of the finest level varies from 0.2% to 0.003%. The third run has three levels of refinement with the grid sizes of 128^3 at the coarsest level, 256^3 at the intermediate level, and 512^3 at the finest level. The density of the finest level ranges from 0.87% to 0.90%.

Note that the density of the finest level describes how much of the data in the dataset is at the highest resolution; a higher density of the finest level means that more data is refined to the highest resolution. Usually, the data density is gradually increasing at the finest level, within a single run.

Evaluation platform and compressor. The test platform is equipped with two 28-core Intel Xeon Gold 6238R processors and 384 GB of memory. We use SZ3 [40], which is easy to (de)couple lossless encoding from SZ compression, due to its high modularity.

TABLE 1: Our tested datasets.

Dataset	# Levels	Grid Size of Each Level (Fine to Coarse)	Density of Each Level (Fine to Coarse)
Nyx_Run1_Z10	2	512, 256	23%, 77%
Nyx_Run1_Z5	2	512, 256	58%, 42%
Nyx_Run1_Z2	2	512, 256	63%, 37%
Nyx_Run2_T2	2	256, 128	0.2%, 99.8%
Nyx_Run2_T3	3	512, 256, 128	0.02%, 0.56%, 99.42%
Nyx_Run2_T4	4	1024, 512, 256, 128	3E-5, 0.02%, 2.2%, 97.7%
Nyx_Run3_Z1.5	3	512, 256, 128	0.87%, 13.88%, 85.25%
Nyx_Run3_Z1	3	512, 256, 128	0.90%, 14.70%, 84.40%

Comparison baselines. As discussed in Section 2, we have three 1D or 3D comparison baselines. Specifically, (1) the 1D baseline (*naive*): each AMR level is compressed separately as a 1D array; (2) the 1D baseline (*zMesh*) [27]: we refer readers to Section 2 for more details about how the zMesh approach reorganize the AMR data for 1D compression; and (3) the 3D baseline: Different AMR levels are unified to the same resolution for 3D compression; (4) the TAC baseline: each AMR level is compressed using OpST (without SHE), AKDTree

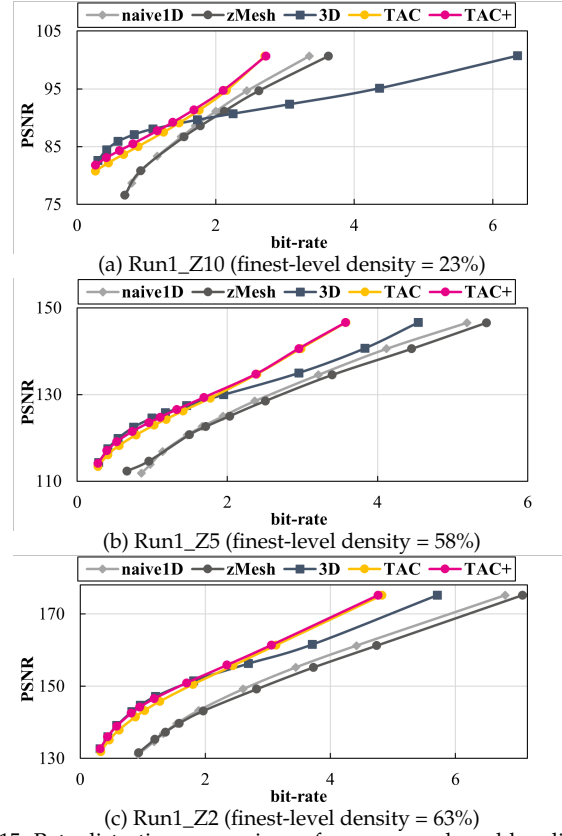


Fig. 15: Rate-distortion comparison of our approach and baselines on the early time-step (Z10) to the late time-step (Z2) from Nyx run1.

(without SHE), and GSP based on the data density. For more information, we refer readers to [41] for more details.

4.2 Evaluation Metrics

We will evaluate the compression performance based on the following metrics: (1) compression ratio or bit-rate (generic), (2) distortion quality (generic), (3) compression throughput (generic), (4) rate-distortion (generic), (5) power spectrum (cosmology specific), (6) Halo finder (cosmology specific).

Metric 1: To evaluate the size reduction as a result of the compression, we use the compression ratio, defined as the ratio of the original data size compared to the compressed data size, or bit-rate (bits/value), representing the amortized storage cost of each value. For single/double floating-point data, the bit-rate is 32/64 bits per value before compression. The compression ratio and bit-rate have a mathematical relationship as their multiplication is 32/64 so that a lower bit rate means a higher compression ratio.

Metric 2: Distortion is another important metric used to evaluate lossy compression quality. We use the peak signal-to-noise ratio (PSNR) to measure the distortion quality.

$$\text{PSNR} = 20 \cdot \log_{10}(R_X) - 10 \cdot \log_{10}\left(\frac{\sum_{i=1}^N e_i^2}{N}\right),$$

where e_i is the difference between the original and decompressed values for the point i , N is the number of points, and R_X is the value range of X . Higher PSNR less error.

Metric 3: (De)compression throughputs are critical to improving the I/O performance. We calculate the throughput based on the original data size and (de)compression time.

Metric 4: Similar to prior work [14], [15], [42], [32], [20], [43], [35], we plot the rate-distortion curve to compare the

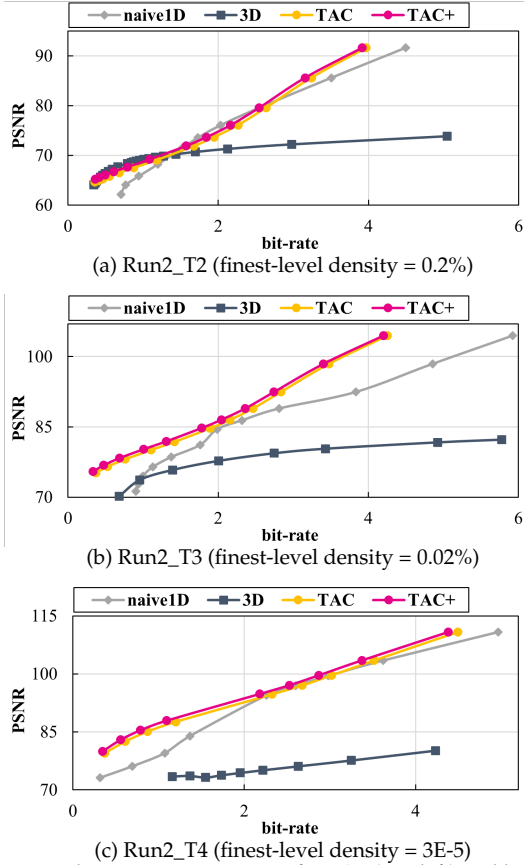


Fig. 16: Rate-distortion comparison of TAC+ (top-left) and baselines on different time-steps from run2.

distortion quality with the same bit-rate, for a fair comparison between different compression approaches, taking into account diverse compression algorithms.

Metric 5: Matter distribution in the Universe has evolved to form astrophysical structures on different physical scales, from planets to larger structures such as superclusters and galaxy filaments. The two-point correlation function $\xi(r)$, which gives the excess probability of finding a galaxy at a certain distance r from another galaxy, statistically describes the amount of the Universe at each physical scale. The Fourier transform of $\xi(r)$ is called the matter power spectrum $P(k)$, where k is the comoving wavenumber. The matter power spectrum describes how much structure exists at each physical scale. We run the power spectrum on the baryon density field by using a cosmology analysis tool called Gimlet. We compare the power spectrum $p'(k)$ of decompressed data with the original $p(k)$ and accept a maximum relative error within 1% for all $k < 10$.

Metric 6: Halo finder aims to find the halos (overdensities) in the dark matter distribution and output the positions, the number of cells, and the mass for each halo it finds, respectively. Specifically, the halo-finder algorithm [44] searches for the halos from all the simulated data, with the following two criteria: (1) the mass of a data point must be greater than a threshold (e.g., $81.66\times$ of the average mass of the whole dataset) to become a halo cell candidate [20], [43], [45], and (2) there must be enough halo cell candidates in a certain area to form a halo. For decompressed data, some of the information (mass and cells of halos) can be distorted from the original.

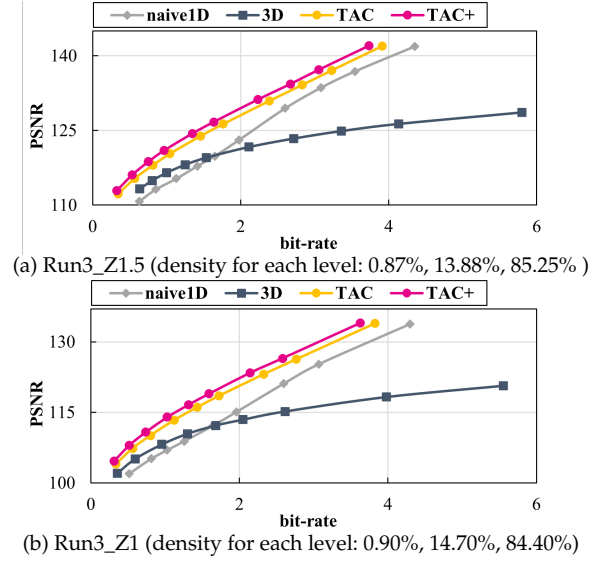


Fig. 17: Rate-distortion comparison of our approach and baselines on different time-steps from Nyx run3.

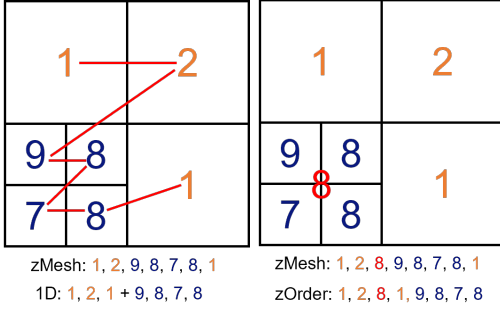
4.3 Evaluation on Rate-distortion

We first evaluate the rate-distortion of our proposed compression approach and compare it with the baselines on different datasets. As shown in Figure 15, 16 and 17, our new approach with SHE, TAC+ (represented by the pink curve) yields better performance than the original TAC (the yellow curve) without SHE. Also, for the 1D baseline, our approach (top-left curve) outperforms the 1D baseline across all 8 datasets. Furthermore, the performance of our approach is more stable (i.e., smoother curve) than the 1D baseline. We can also find that zMesh is slightly worse than the 1D baseline on our tested data as shown in Figure 15, which will be explained in the next section.

For the 3D baseline, we observe that our solution has much better performance when the finest level has a relatively low density or the decompressed data has a high PSNR, as shown in Figure 15, 16 and 17. However, our approach cannot dominate the 3D baseline as shown in Figure 15a, 15b, and 16a, when the following criteria are satisfied: (1) the AMR data has only two levels of refinement, (2) the finest level has a relatively low density, and (3) the decompressed data has low PSNR/bitrate.

We also find that as the finest level density increases, the bitrate threshold where the 3D baseline performs better than TAC+ is increasing, while the advantage of the 3D baseline over TAC+ is decreasing, as shown in Figure 15 and 16a. Specifically, in Figure 16a (the finest level density is 0.2%), TAC+ outperforms the 1D baseline when the bit-rate is above 1.2; in Figure 15a (the finest level density is 23%), the intersection is the bit-rate of 1.25; as the finest level density continues to grow up to 58% in Figure 15c, TAC+ is slightly worse than the 3D baseline until the bit-rate is larger than 1.5; when the finest level density reaches 63% in Figure 15c, TAC+ and the 3D baseline yield (almost) the same performance.

In the next section, we will discuss how the number of AMR levels, the density of the finest level, and the bit-rate/PSNR of decompressed data affect the performance of the 3D baseline and TAC+ in detail.



(a) Tree-based AMR data (b) Patch-based AMR data

Fig. 18: An example of how the 1D baseline, zMesh, and original z-order reorder a simple 2D AMR data without and with redundancy. Orange: coarse level, blue: fine level, red: redundant data.

4.4 Discussion on Comparison with Baselines

On compression, zMesh is meant to improve the smoothness of the patch-based AMR datasets by taking advantage of the data redundancy between each AMR level (as described in the introduction). Thus, zMesh cannot improve the smoothness if there is no data redundancy in the tree-structured AMR datasets (i.e., our tested datasets). A simple example is used to illustrate this in Figure 18b, where the finer-level data has higher values because a grid will be refined only if its value is larger than a certain threshold. For block-based AMR, when a grid needs to be refined because of its high value, the value will still remain in the level, resulting in a redundant value saved (i.e., the red 8). If one uses the original z-ordering to traverse the data level-by-level (shown in Figure 18b), the reordered data will have three significant value changes (i.e., from 2 to 8, from 8 to 1, and from 1 to 9). To solve this issue, zMesh traverses the two AMR levels together based on the layout of the 2D array. The reordered data are “1-2-8-9-8-7-8-1”, which only has two significant value changes (i.e., from 2 to 8 and from 8 to 1). Thus, zMesh can improve the smoothness of patch-based AMR data.

However, as shown in Figure 18a, for tree-structured AMR data (without saving a redundant “8”), compared to the 1D baseline that compresses each level separately, zMesh introduces two significant data changes (i.e., from 2 to 9 and from 8 to 1) as it traverses between two AMR levels. This explains why zMesh is slightly worse than the 1D baseline on our data.

When considering the 3D baseline, we observe that it works slightly better than TAC+ in the following circumstances: (1) the AMR data has only two levels of refinement, (2) the decompressed data has a low PSNR/bit-rate, and (3) the finest level of the data has a relatively low density. We also observe that (4) when the finest level density increases, the bit-rate intersection point where the 3D baseline performs better than TAC+ shifts to a higher value, (5) while the advantage of the 3D baseline over TAC+ becomes smaller.

We now explain each observation point individually. As mentioned in Section 2.4, the main disadvantage of the 3D baseline is the redundant data generated by the up-sampling process, which becomes more significant for the AMR data with more than two levels of refinement, resulting in poor compression performance (point 1). In contrast, the 3D baseline has better data locality and smoothness over TAC+ because it compresses the entire dataset together without partitioning the data. This leads to better compressibility for the 3D baseline, resulting in faster bitrate reduction and

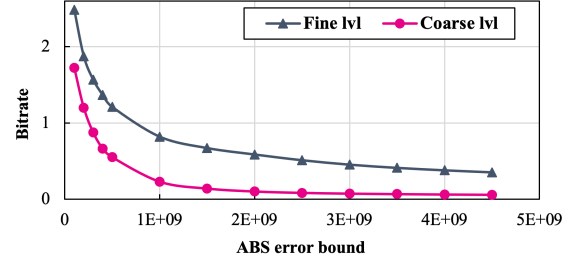


Fig. 19: Bit-rates with different error bounds using SZ lossy compression for fine and coarse levels on Run1_ZZ dataset.

slower PSNR degradation when the error bound increases, compared to TAC+. As a result, the 3D baseline performs better at a low bit-rate (point 2).

However, when the finest level density increases, the smoothness advantage of the 3D baseline will decrease. This is because TAC+ will have more data located in the finest level, and the partition overhead of TAC+ is lower at the finest level compared to coarser levels due to the larger (unit) block size. This explains why the 3D baseline only outperforms TAC+ for AMR datasets with low density (points 3 & 5). Also, note that for the dataset with low density in the finest level, the overhead of redundant up-sampled data will be high for the 3D baseline, especially for high bit-rates (because the 3D baseline only has better smoothness in low bit-rates). Thus, the compression performance of the 3D baseline will decrease rapidly as we aim for relatively high PSNRs/bit-rates, leading to a smaller intersection bit-rate between the 3D baseline and TAC+. Clearly, as the finest level density increases, the overhead of the redundant data will be smaller, resulting in a larger intersection bit-rate between the 3D baseline and TAC+ (point 4).

4.5 Post-analysis Quality with Adaptive Error Bound

When factoring level-wise compression, our approach can apply different error bounds to different AMR levels based on (1) the post-analysis metrics, (2) the up-sampling rates of coarse levels, and (3) the rate-distortion trade-off between different AMR levels. We now evaluate our approach with the two cosmology-specific post-analysis metrics (i.e., power spectrum and halo finder) to demonstrate the benefit of the adaptive error bound method. We choose the dataset run1-Z2 for evaluation because TAC+ has a similar performance as the 3D baseline on this dataset.

Figure 19 shows the motivation of performing rate-distortion trade-off between different AMR levels. As the error bounds for the fine and coarse levels increase, their bit rates will converge to a similar value. This means that when the error bound is relatively large, the reduction in data size will be insignificant compared to the compression error increment (i.e., the slopes of both curves are very small). Therefore, we can say that when the error is large, it is not worth trading data quality for size reduction.

Power Spectrum Figure 20a shows that under the (almost) same compression ratio, TAC+ (with the uniform error bound) has a better power-spectrum error compared to the 3D baseline. Also note that TAC+ yields nearly lossless power-spectrum distortion (less than 0.01%) under the compression ratio of 42 \times , as shown in Figure 20a’s gray curve.

Now, let us follow the three steps mentioned at the beginning of this section to adjust the error bound for each AMR

TABLE 2: Overall compression/decompression throughput (MB/s) of different approaches with different absolute error bounds.

EB_abs	Run1_Z10				Run1_Z2				Run2_T2				Run2_T4				Run3_Z1			
	1D	3D	TAC	TAC+	1D	3D	TAC	TAC+	1D	3D	TAC	TAC+	1D	3D	TAC	TAC+	1D	3D	TAC	TAC+
1E+08	51	37	79	77	51	79	85	84	71	15	71	66	49	0.32	24	24	49	5.6	63	63
1E+09	81	48	94	93	55	92	103	97	79	21	85	79	53	0.39	26	26	53	6.5	78	75
1E+10	89	53	107	102	58	100	111	104	86	23	98	87	84	0.41	28	27	57	7.1	91	84

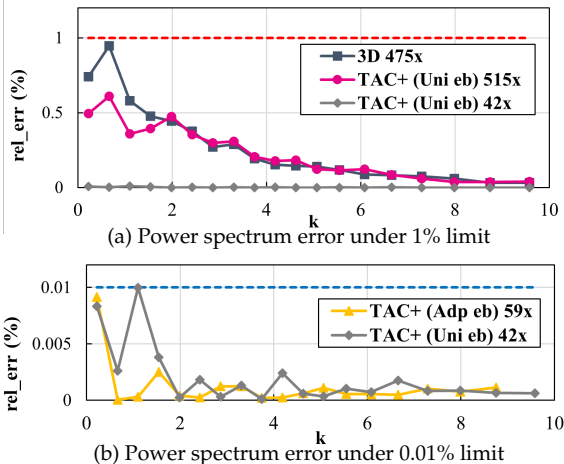


Fig. 20: Power spectrum error (in relative) of the 3D baseline and TAC+ (uniform error bound) and TAC+ (adaptive error bound) on baryon density field on run1-Z2. The red and blue dashed line is the 1% and 0.01% limit of acceptable power spectrum error.

level. First, the post-analysis metric—power spectrum—needs to be run on the uniform-resolution data and focuses on the global quality of data. Thus, the ideal error-bound configuration/ratio for the fine and coarse levels on the uniform-resolution data would be 1:1.

As aforementioned, the coarse level of the AMR dataset needs to be up-sampled to uniform the resolution. As a result, the compression error of the coarse level will be up-sampled as well, resulting in more error in the post-analysis. Thus, we then need to give the coarse level a smaller error bound based on the up-sample rate. Here the up-sample rate for Z2’s coarse level is 2^3 , leading to an ideal error-bound ratio of the fine and coarse levels changed to 8:1.

Finally, this 8:1 ratio needs to be adjusted based on the rate-distortion trade-off as aforementioned. As shown in Figure 19, when using the error-bound ratio of 8:1 (e.g., $4E+9$ for the fine level and $5E+8$ for the coarse level), the error bound of the fine level is too large, resulting in an ineffective rate-distortion trade-off. Thus, we can balance two levels by increasing the error bound for the coarse level (to gain compression ratio) and decreasing the error bound for the fine level (to add compression error), which can achieve an overall rate-distortion benefit. Based on our experiments, we adjust the error-bound ratio from 8:1 to 3:1. As shown in Figure 20b, TAC+ with adaptive error bound can significantly improve the compression ratio compared with uniform error bound under similar power spectrum error.

Halo finder We evaluate the mass change, and the number of cells change for the three largest halos identified using the 3D baseline, TAC+ (with uniform error bound), and TAC+ (with adaptive error bound), as shown in Table 3. We can see that TAC+ with uniform error bound produces better halo-finder analysis quality than the 3D baseline.

Similar to the error-bound configuration analysis done for the power spectrum, let us now adjust the error-bound ratio between the fine and coarse levels for halo finder. The

TABLE 3: Halo finder analysis with different methods.

	CR	Avg Rel Mass Diff	Avg Rel Cells Diff
3D baseline	188.7	2.7E-04	2.2E-03
TAC+ (1:1)	189.1	2.2E-04	2.1E-03
TAC+ (2:1)	192.5	1.1E-04	9.0E-04

halo-finder analysis also requires uniform-resolution data as input. However, different from the power-spectrum analysis, the halo-finder analysis focuses more on high-value points at the fine level, since only high-value data points qualify as halo candidates, as described in Section 4.2. Note that this does not mean we can directly discard the coarse-level data with small values as they still contribute to the average value of the dataset, which is also an important parameter for the halo finder [44]. Therefore, we set the ideal error-bound ratio to 1:2 (i.e., fine level vs coarse level) for the uniform-resolution data based on our massive experiments. After that, considering the up-sampling rate of 2^3 , the error-bounded ratio is changed to 4:1. Finally, we adjust the ratio to 2:1 based on the rate-distortion trade-off. Table 3 shows that TAC+ with adaptive error bound obtains the minimal differences of the mass and cell numbers.

4.6 Evaluation on Time Overhead

We evaluate the overall throughput (including preprocessing and (de)compression) on the datasets with different error bounds. Compared to the 3D baseline, the throughput of TAC+ is up to $11.8\times$ higher on the Run3 dataset, $75\times$ higher on the Run2 datasets, and $2\times$ higher on the Run1 datasets. This is because the Run2 and Run3 datasets have a lower density than the Run1 datasets at the finest level, resulting in a higher overhead of redundant data for the 3D baseline, which is consistent with our discussion in Section 4.4.

We note that TAC+ performs better than the 1D baseline on all the tested datasets except the T4 datasets, due to its relatively long data-partition time compared to the total time on the small-sized datasets. TAC+ has almost the same throughput as TAC. The very slight decrease is because TAC+ compresses the data in a more fine-grained manner. We exclude zMesh in this evaluation as it is theoretically slower than the 1D baseline due to the extra z-ordering and provides worse rate-distortion according to our evaluation.

5 CONCLUSION AND FUTURE WORK

In conclusion, this paper leverages 3D compression for AMR data on a systemic level. We propose three pre-processing strategies that can adapt based on the density of each AMR level. Our approach improves the compression ratio compared to the state-of-the-art approach by up to $4.9\times$ under the same data quality loss. With our level-wised compression approach, we are able to tune the error-bound ratio of fine and coarse levels to be 3:1 and 2:1 for better power-spectrum and halo-finder analyses, respectively, under the same compression ratio. In future work, we will apply TAC+ to more AMR simulations and improve its throughput on multi-core CPUs using OpenMP and GPUs using CUDA.

REFERENCES

- [1] C. Burstedde, O. Ghattas, G. Stadler, T. Tu, and L. C. Wilcox, "Towards adaptive mesh pde simulations on petascale computers," *Proceedings of Teragrid*, vol. 8, 2008.
- [2] A. Dubey, A. Almgren, J. Bell, M. Berzins, S. Brandt, G. Bryan, P. Colella, D. Graves, M. Lijewski, F. Löffler *et al.*, "A survey of high level frameworks in block-structured adaptive mesh refinement packages," *Journal of Parallel and Distributed Computing*, vol. 74, no. 12, pp. 3217–3227, 2014.
- [3] W. Zhang, A. Almgren, V. Beckner, J. Bell, J. Blaschke, C. Chan, M. Day, B. Friesen, K. Gott, D. Graves *et al.*, "Amrex: a framework for block-structured adaptive mesh refinement," *Journal of Open Source Software*, vol. 4, no. 37, pp. 1370–1370, 2019.
- [4] J. M. Stone, K. Tomida, C. J. White, and K. G. Felker, "The athena++ adaptive mesh refinement framework: Design and magnetohydrodynamic solvers," *The Astrophysical Journal Supplement Series*, vol. 249, no. 1, p. 4, 2020.
- [5] A. S. Almgren, J. B. Bell, M. J. Lijewski, Z. Lukić, and E. Van Andel, "Nyx: A massively parallel amr code for computational cosmology," *The Astrophysical Journal*, vol. 765, no. 1, p. 39, 2013.
- [6] B. Runnels, V. Agrawal, W. Zhang, and A. Almgren, "Massively parallel finite difference elasticity using block-structured adaptive mesh refinement with a geometric multigrid solver," *Journal of Computational Physics*, vol. 427, p. 110065, 2021.
- [7] S. Whitman, J. Brasseur, and P. Hamlington, "Simulation of bluff-body stabilized flames with pelec, an exascale combustion code," 2018.
- [8] K. Sverdrup, N. Nikiforakis, and A. Almgren, "Highly parallelisable simulations of time-dependent viscoplastic fluid flow with structured adaptive mesh refinement," *Physics of Fluids*, vol. 30, no. 9, p. 093102, 2018.
- [9] Nyx, <https://github.com/AMReX-Astro/Nyx>, 2021.
- [10] P. Deutsch, "Gzip file format specification version 4.3," 1996.
- [11] Zstandard, <http://facebook.github.io/zstd/>, 2020.
- [12] S. W. Son, Z. Chen, W. Hendrix, A. Agrawal, W.-k. Liao, and A. Choudhary, "Data compression for the exascale computing era-survey," *Supercomputing Frontiers and Innovations*, vol. 1, no. 2, pp. 76–88, 2014.
- [13] S. Di and F. Cappelto, "Fast error-bounded lossy hpc data compression with sz," in *2016 IEEE international parallel and distributed processing symposium (ipdps)*. IEEE, 2016, pp. 730–739.
- [14] D. Tao, S. Di, Z. Chen, and F. Cappelto, "Significantly improving lossy compression for scientific data sets based on multidimensional prediction and error-controlled quantization," in *2017 IEEE International Parallel and Distributed Processing Symposium (IPDPS)*. IEEE, 2017, pp. 1129–1139.
- [15] X. Liang, S. Di, D. Tao, S. Li, S. Li, H. Guo, Z. Chen, and F. Cappelto, "Error-controlled lossy compression optimized for high compression ratios of scientific datasets," in *2018 IEEE International Conference on Big Data*. IEEE, 2018.
- [16] P. Lindstrom, "Fixed-rate compressed floating-point arrays," *IEEE Transactions on Visualization and Computer Graphics*, vol. 20, no. 12, pp. 2674–2683, 2014.
- [17] M. Ainsworth, O. Tugluk, B. Whitney, and S. Klasky, "Mgard: A multilevel technique for compression of floating-point data," in *DRBSD-2 Workshop at Supercomputing*, 2017.
- [18] R. Ballester-Ripoll, P. Lindstrom, and R. Pajarola, "Tthresh: Tensor compression for multidimensional visual data," *IEEE Transactions on Visualization and Computer Graphics*, vol. 26, no. 9, pp. 2891–2903, 2020.
- [19] F. Cappelto, S. Di, S. Li, X. Liang, A. M. Gok, D. Tao, C. H. Yoon, X.-C. Wu, Y. Alexeev, and F. T. Chong, "Use cases of lossy compression for floating-point data in scientific data sets," *The International Journal of High Performance Computing Applications*, 2019.
- [20] S. Jin, P. Grosset, C. M. Biwer, J. Pulido, J. Tian, D. Tao, and J. Ahrens, "Understanding gpu-based lossy compression for extreme-scale cosmological simulations," in *2020 IEEE International Parallel and Distributed Processing Symposium (IPDPS)*. IEEE, 2020, pp. 105–115.
- [21] P. Grosset, C. M. Biwer, J. Pulido, A. T. Mohan, A. Biswas, J. Patchett, T. L. Turton, D. H. Rogers, D. Livescu, and J. Ahrens, "Foresight: analysis that matters for data reduction," in *SC20: International Conference for High Performance Computing, Networking, Storage and Analysis*. IEEE, 2020, pp. 1–15.
- [22] T. Lu, Q. Liu, X. He, H. Luo, E. Suchyta, J. Choi, N. Podhorszki, S. Klasky, M. Wolf, T. Liu *et al.*, "Understanding and modeling lossy compression schemes on hpc scientific data," in *2018 IEEE International Parallel and Distributed Processing Symposium (IPDPS)*. IEEE, 2018, pp. 348–357.
- [23] A. H. Baker, H. Xu, J. M. Dennis, M. N. Levy, D. Nychka, S. A. Mickelson, J. Edwards, M. Vertenstein, and A. Wegener, "A methodology for evaluating the impact of data compression on climate simulation data," in *Proceedings of the 23rd International Symposium on High-Performance Parallel and Distributed Computing*. ACM, 2014, pp. 203–214.
- [24] A. H. Baker, H. Xu, D. M. Hammerling, S. Li, and J. P. Clyne, "Toward a multi-method approach: Lossy data compression for climate simulation data," in *International Conference on High Performance Computing*. Springer, 2017, pp. 30–42.
- [25] A. M. Gok, S. Di, Y. Alexeev, D. Tao, V. Mironov, X. Liang, and F. Cappelto, "Pastri: Error-bounded lossy compression for two-electron integrals in quantum chemistry," in *2018 IEEE international conference on cluster computing (CLUSTER)*. IEEE, 2018, pp. 1–11.
- [26] X.-C. Wu, S. Di, E. M. Dasgupta, F. Cappelto, H. Finkel, Y. Alexeev, and F. T. Chong, "Full-state quantum circuit simulation by using data compression," in *Proceedings of the International Conference for High Performance Computing, Networking, Storage and Analysis*, 2019, pp. 1–24.
- [27] H. Luo, J. Wang, Q. Liu, J. Chen, S. Klasky, and N. Podhorszki, "zmesh: Exploring application characteristics to improve lossy compression ratio for adaptive mesh refinement," in *2021 IEEE International Parallel and Distributed Processing Symposium (IPDPS)*. IEEE, 2021, pp. 402–411.
- [28] G. K. Wallace, "The JPEG still picture compression standard," *IEEE Transactions on Consumer Electronics*, vol. 38, no. 1, pp. xviii–xxxiv, 1992.
- [29] D. Le Gall, "Mpeg: A video compression standard for multimedia applications," *Communications of the ACM*, vol. 34, no. 4, pp. 46–58, 1991.
- [30] "2021 r&d 100 award winners," <https://www.rdworldonline.com/rd-100-2021-winner/sz-a-lossy-compression-framework-for-scientific-data/>, 2021.
- [31] K. Zhao, S. Di, M. Dmitriev, T.-L. D. Tonellot, Z. Chen, and F. Cappelto, "Optimizing error-bounded lossy compression for scientific data by dynamic spline interpolation," in *2021 IEEE 37th International Conference on Data Engineering*. IEEE, 2021, pp. 1643–1654.
- [32] X. Liang, Q. Gong, J. Chen, B. Whitney, L. Wan, Q. Liu, D. Pugmire, R. Archibald, N. Podhorszki, and S. Klasky, "Error-controlled, progressive, and adaptable retrieval of scientific data with multilevel decomposition," in *Proceedings of the International Conference for High Performance Computing, Networking, Storage and Analysis*, 2021, pp. 1–13.
- [33] F. Wang, N. Marshak, W. Usher, C. Burstedde, A. Knoll, T. Heister, and C. Johnson, "Cpu ray tracing of tree-based adaptive mesh refinement data," *Computer Graphics Forum*, vol. 39, pp. 1–12, 06 2020.
- [34] G. Harel, J.-B. Lekien, and P. Pébay, "Two new contributions to the visualization of amr grids: I. interactive rendering of extreme-scale 2-dimensional grids ii. novel selection filters in arbitrary dimension," 03 2017.
- [35] K. Zhao, S. Di, X. Liang, S. Li, D. Tao, Z. Chen, and F. Cappelto, "Significantly improving lossy compression for hpc datasets with second-order prediction and parameter optimization," in *Proceedings of the 29th International Symposium on High-Performance Parallel and Distributed Computing*, 2020, pp. 89–100.
- [36] J. Bentley, "Multidimensional binary search trees used for associative searching," *communications of the ACM September, 1975. vol. 18: pp. 509-517 : ill. includes bibliography.*, vol. 18, 01 1975.
- [37] D. Hoang, H. Bhatia, P. Lindstrom, and V. Pascucci, "High-quality and low-memory-footprint progressive decoding of large-scale particle data," in *2021 IEEE 11th Symposium on Large Data Analysis and Visualization (LDAV)*. IEEE Computer Society, 2021, pp. 32–42.
- [38] G. Cirio, G. Lavoué, and F. Dupont, "A framework for data-driven progressive mesh compression," in *GRAPP*, 2010, pp. 5–12.
- [39] O. Devillers and P.-M. Gandoin, "Geometric compression for interactive transmission," *Proc. Visualization '00*, 01 2000.
- [40] X. Liang, K. Zhao, S. Di, S. Li, R. Underwood, A. M. Gok, J. Tian, J. Deng, J. C. Calhoun, D. Tao, Z. Chen, and F. Cappelto, "Sz3: A modular framework for composing prediction-based error-bounded lossy compressors," *IEEE Transactions on Big Data*, pp. 1–14, 2022.
- [41] D. Wang, J. Pulido, P. Grosset, S. Jin, J. Tian, J. Ahrens, and D. Tao, "Tac: Optimizing error-bounded lossy compression for three-dimensional adaptive mesh refinement simulations," in *Pro-*

ceedings of the 31st International Symposium on High-Performance Parallel and Distributed Computing, 2022, p. 135–147.

- [42] X. Liang, S. Di, D. Tao, Z. Chen, and F. Cappello, “An efficient transformation scheme for lossy data compression with point-wise relative error bound,” in *2018 IEEE International Conference on Cluster Computing (CLUSTER)*. IEEE, 2018, pp. 179–189.
- [43] S. Jin, J. Pulido, P. Grosset, J. Tian, D. Tao, and J. Ahrens, “Adaptive configuration of in situ lossy compression for cosmology simulations via fine-grained rate-quality modeling,” in *Proceedings of the 30th International Symposium on High-Performance Parallel and Distributed Computing*, 2021, pp. 45–56.
- [44] M. Davis, G. Efstathiou, C. S. Frenk, and S. D. White, “The evolution of large-scale structure in a universe dominated by cold dark matter,” *The Astrophysical Journal*, vol. 292, pp. 371–394, 1985.
- [45] B. Fang, D. Wang, S. Jin, Q. Koziol, Z. Zhang, Q. Guan, S. Byna, S. Krishnamoorthy, and D. Tao, “Characterizing impacts of storage faults on hpc applications: A methodology and insights,” in *2021 IEEE International Conference on Cluster Computing (CLUSTER)*. IEEE, 2021, pp. 409–420.



Daocce Wang is a PhD student in Intelligent Systems Engineering at Indiana University Bloomington. He received his bachelor's degree in Computer Science from University of Electronic Science and Technology of China in 2018 and his master's degree in Computer Science from University of Florida in 2020. His research interests include scientific data reduction, AMR simulations, and parallel algorithms.



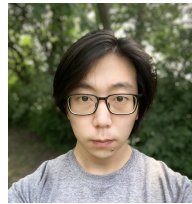
Jesus Pulido is a research scientist in the Data Science at Scale Team at Los Alamos National Laboratory. Pulido received his Ph.D. in Computer Science at University of California, Davis in 2019. Pulido specializes in data analysis, data reduction, visualization, high performance computing, wavelets and multi-resolution methods. He has experience in applications of image sensors, astronomy, turbulence and cosmology.



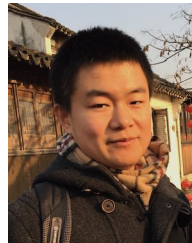
Pascal Grosset is a scientist in the Data Science at Scale team at Los Alamos National Laboratory. His primary research interests are large-scale data analysis and visualization, and data reduction. He received his Ph.D. in Computing: Graphics and Visualization from the University of Utah in 2016 where his research focused on large scale visualization.



Sian Jin is currently working toward the PhD degree majoring in computer engineering at Indiana University Bloomington. His research interests include High Performance Computing, Compression Algorithms, Artificial Neural Networks, and Parallel Computing. He has published several papers in major journals and international conferences including the SC, PPOPP, VLDB, HPDC, IPDPS, and ICDE.



Jiannan Tian is a PhD candidate in Intelligent Systems Engineering at Indiana University Bloomington. His research interests include lossy compression for scientific data and error analysis, and GPU-centric computing. His ongoing project including developing GPU-accelerated compression algorithm and system design optimization of lossy compression.



Kai Zhao is an assistant professor of computer science at University of Alabama at Birmingham. He received his Ph.D. in computer science from University of California, Riverside in 2022. He received his bachelor's degree from Peking University in 2014. His research interests include high-performance computing, scientific data management and reduction, and resilient machine learning.



James P. Ahrens received the BS degree in computer science from the University of Massachusetts at Amherst, Amherst, Massachusetts, in 1989, and the PhD degree in computer science from the University of Washington, Seattle, Washington, in 1996. He is a senior scientist with Applied Computer Science Group, Los Alamos National Laboratory. His primary research interests include visualization, computer graphics, data science, and parallel systems. He is author of more than 100 peer reviewed papers

and the founder/design lead of ParaView, an open-source visualization tool designed to handle extremely large data. ParaView is broadly used for scientific visualization and is in use at supercomputing and scientific centers worldwide. He is the chair of the IEEE Computer Society Technical Committee on Visualization and Graphics (VGTC).



Dingwen Tao is an associate professor at Indiana University Bloomington, where he directs the High-Performance Data Analytics and Computing Lab. He received his Ph.D. in Computer Science from University of California, Riverside in 2018 and B.S. in Mathematics from University of Science and Technology of China in 2013. He is the recipient of various awards including NSF CAREER Award (2023), Amazon Research Award (2022), Meta Research Award (2022), R&D100 Awards Winner (2021), IEEE Computer

Society TCHPC Early Career Researchers Award for Excellence in HPC (2020), NSF CRII Award (2020), and IEEE CLUSTER Best Paper Award (2018). He is serving on the Technical Review Board of IEEE Transactions on Parallel and Distributed Systems. He served as the Program Co-chair of 2021 IEEE International Conference on Scalable Computing and Communications and International Workshops on Big Data Reduction. He is also a reviewer, program committee member, or session chair of major HPC venues, such as SC, HPDC, ICS, IPDPS, CLUSTER, ICPP, CCGrid, and HiPC. Email: ditao@iu.edu.